



# Micelles assembled with carbocyanine dyes for theranostic near-infrared fluorescent cancer imaging and photothermal therapy

Hong Yang<sup>a,1</sup>, Huajian Mao<sup>a,1</sup>, Zhihui Wan<sup>a</sup>, Aijun Zhu<sup>a</sup>, Miao Guo<sup>a</sup>, Yanli Li<sup>a</sup>, Xinming Li<sup>b</sup>, Jiangling Wan<sup>c</sup>, Xiangliang Yang<sup>c</sup>, Xintao Shuai<sup>d</sup>, Huabing Chen<sup>a,\*</sup>

<sup>a</sup> College of Pharmaceutical Sciences, Soochow University, Suzhou, Jiangsu 215123, China

<sup>b</sup> College of Chemistry, Chemical Engineering and Materials Science, Soochow University, Suzhou, Jiangsu 215123, China

<sup>c</sup> College of Life Science and Technology, Huazhong University of Science and Technology, Wuhan 430074, China

<sup>d</sup> Center of Biomedical Engineering, Zhongshan School of Medicine, Sun Yat-sen University, Guangzhou 510275, China

## ARTICLE INFO

### Article history:

Received 10 June 2013

Accepted 9 August 2013

Available online 2 September 2013

### Keywords:

Micelles

Indocyanine green

Cypate

Near-infrared fluorescent imaging

Photothermal therapy

## ABSTRACT

It is an emerging focus to explore a theranostic nanocarrier for simultaneous cancer imaging and therapy. Herein, we demonstrate a theranostic micelle system for cancer near infrared fluorescent (NIRF) imaging with enhanced signal to noise ratio and superior photothermal therapy. The copolymers consisting of monomethoxy poly(ethylene glycol) and alkylamine-grafted poly(L-aspartic acid) are assembled with carbocyanine dyes into theranostic micelles, which exhibit small size, high loading capacity, good stability, sustained release behavior, and enhanced cellular uptake. The micelles achieve the preferable biodistribution and long-term retention of carbocyanine dyes at tumor, which result in enhanced NIRF imaging by generating stable retention of NIRF signals at both hypervascular and hypovascular tumors during a long-term imaging period of up to 8 day, accompanying with negligible noise at normal tissues. The photostability of carbocyanine dye (Cypate) plays an important role for long-term cancer imaging with enhanced SNR. Moreover, the micelles exhibit severe photothermal damage on cancer cells via the destabilization of subcellular organelles upon photoirradiation, causing superior photothermal tumor regress. The micelles act as a powerful theranostic nanocarrier for simultaneous cancer imaging with high contrast and superior photothermal therapy.

© 2013 Elsevier Ltd. All rights reserved.

## 1. Introduction

Theranostic nanocarriers have been considered as an emerging field for personalized medicine [1–3]. Conventional theranostic nanocarriers generally integrate both imaging probe and therapeutic agent to achieve ultrasensitive cancer imaging and simultaneously efficient cancer therapy [4–6]. Recently, bifunctional agents possessing both near infrared fluorescence (NIRF) and therapeutic potential have been considered as promising theranostic agents for multimodal nanomedicine, owing to their low tissue auto-fluorescence, high sensitivity, deep tissue penetration and good anticancer efficiency [7–9]. For instance, some carbocyanine dyes such as indocyanine green (ICG) and Cypate have extensively been explored as clinically attractive theranostic dyes, owing to their ideal NIR absorbance (~780 nm), thereof emission above 800 nm,

and photothermal effect [10–12], which are fascinating for theranostic application [13,14].

So far, several nanocarriers including micelles, polymeric nanoparticles and calcium phosphate nanoparticles have been employed to encapsulate or conjugate carbocyanine dyes for improving their photostability, drug loading capability as well as *in vivo* tumor accumulation [15–18]. However, existing nanocarriers still suffer from several major drawbacks for their theranostic application [17]. Firstly, amphiphilic or hydrophobic carbocyanine dyes such as ICG and Cypate generally exhibit a low drug loading within nanocarriers, and it is highly difficult to achieve desirable encapsulation at a high drug loading using existing biodegradable polymers [9,10,15,19]. Secondly, most probes still display insufficient signal to noise ratio (SNR) because these dyes generally have short imaging period of less than 48 h, and are mainly distributed into normal tissues such as liver and kidney, and subsequently generate strong noise during the short imaging period, even though some cancer-targeted nanocarriers have been employed [11,15,16]. Thirdly, existing studies mainly focused on permeable hypervascular tumors for cancer imaging [15,20], and

\* Corresponding author.

E-mail address: [chenhb@suda.edu.cn](mailto:chenhb@suda.edu.cn) (H. Chen).

<sup>1</sup> These authors contributed equally.

there is a lack of report on poorly permeable hypovascular tumor, in which nanocarrier may encounter poor penetration and low accumulation [21]. Finally, it is still unknown possibility to apply carbocyanine dyes for *in vivo* cancer photothermal therapy via intravenous administration, even though some nanoparticles encapsulating ICG have been explored for their *in vitro* photothermal effect [9,11]. Consequently, it is highly desirable to develop a clinically potential nanocarrier with effective assembly of carbocyanine dyes for achieving enhanced cancer imaging with high SNR and simultaneously superior photothermal therapy. Herein, we constructed a new polyaspartamide-based micelle system with multiple advantages including small size, high loading capacity, good stability, sustained release and enhanced cellular uptake (Scheme 1). The micelles were used to assemble with carbocyanine dyes for enhanced NIRF cancer imaging. Simultaneously, the micelles were further exploited to generate superior photothermal effect on cancer cells, and achieve efficient photothermal efficacy upon photoirradiation.

## 2. Materials and methods

### 2.1. Materials

$\beta$ -benzyl-L-aspartate N-carboxyanhydride (BLA-NCA) was obtained from Enlai Biological Technology Company (Chengdu, China). mPEG-NH<sub>2</sub> (12,000 MW) was purchased from Jenkem Technology Company (Beijing, China). mPEG-*b*-PASP was synthesized as mentioned in the reference (The degree of polymerization of PASp segment was calculated to be 64 according to <sup>1</sup>H NMR spectrum, Fig. S1) [22]. Cy5-NHS and Cy7.5-NHS were obtained from Lumiprobe (USA). Cypate was synthesized as reported in the references [23,24]. Hoechst 33342 and LysoTracker Green DND-26 were purchased from Invitrogen. ICG, decylamine and tetradecylamine were obtained from Sigma–Aldrich. Octylamine was purchased from Alfa Aesar.

### 2.2. Synthesis and preparation

mPEG-*b*-PASP was reacted with octylamine, decylamine and tetradecylamine in anhydrous N-methyl pyrrolidone (NMP) at 45 °C overnight, respectively. Then, the solutions were dialyzed in the mixture of ethanol and water to remove excess amines and then dialyzed in water. Finally, mPEG-*b*-PASP(OA), mPEG-*b*-PASP(DA), and mPEG-*b*-PASP(TA) were obtained by lyophilizing the dialyzed solutions, and their degrees of polymerization were calculated to be 52, 53 and 52 respectively according to <sup>1</sup>H NMR spectrums. Cy5-labeled mPEG-*b*-PASP(DA) (mPEG-*b*-PASP(DA)-Cy5) and Cy7.5-labeled PEG-*b*-PASP(DA) (mPEG-*b*-PASP(DA)-Cy7.5) were synthesized by conjugating mPEG-*b*-PASP(DA) with Cy5-NHS and Cy7.5-NHS, respectively.

ICG was mixed with mPEG-*b*-PASP(OA), mPEG-*b*-PASP(DA), and mPEG-*b*-PASP(TA) at the ratio of 1:4 in CH<sub>2</sub>Cl<sub>2</sub> respectively, and then the solutions were evaporated using rotary evaporator. Subsequently, the micelles including ICG-OA-M, ICG-DA-M and ICG-TA-M were prepared by dispersing the evaporated mixtures in de-ionized water, respectively. Cy5-labeled ICG-DA-M was prepared by replacing mPEG-*b*-PASP(DA) with mPEG-*b*-PASP(DA)-Cy5 according to the above procedures. The empty Cy7.5-labeled mPEG-*b*-PASP(DA) micelles were prepared by dispersing mPEG-*b*-PASP(DA)-Cy7.5 into water. To prepare Cy-DA-M, mPEG-*b*-PASP(DA) and Cypate at the ratio of 1:1 were dissolved in DMSO, and then dispersed into water. Finally, Cy-DA-M was prepared by dialyzing the solution in water.

### 2.3. Characterization

Dynamic light scattering (DLS, Malvern, UK) was used to measure the hydrodynamic diameter of micelles at 25 °C. The morphology was observed on SPA 400 Atom force Microscope (Seiko, Japan). The absorption and fluorescent spectrums of ICG or Cypate were measured using UV–vis Spectrophotometer (UV2600, Shimadzu) and Fluorescence Spectrophotometer (LS 55, Perkin Elmer). Cy-DA-M was observed using scanning electron microscopy (S-4700, Hitachi).

### 2.4. Drug release

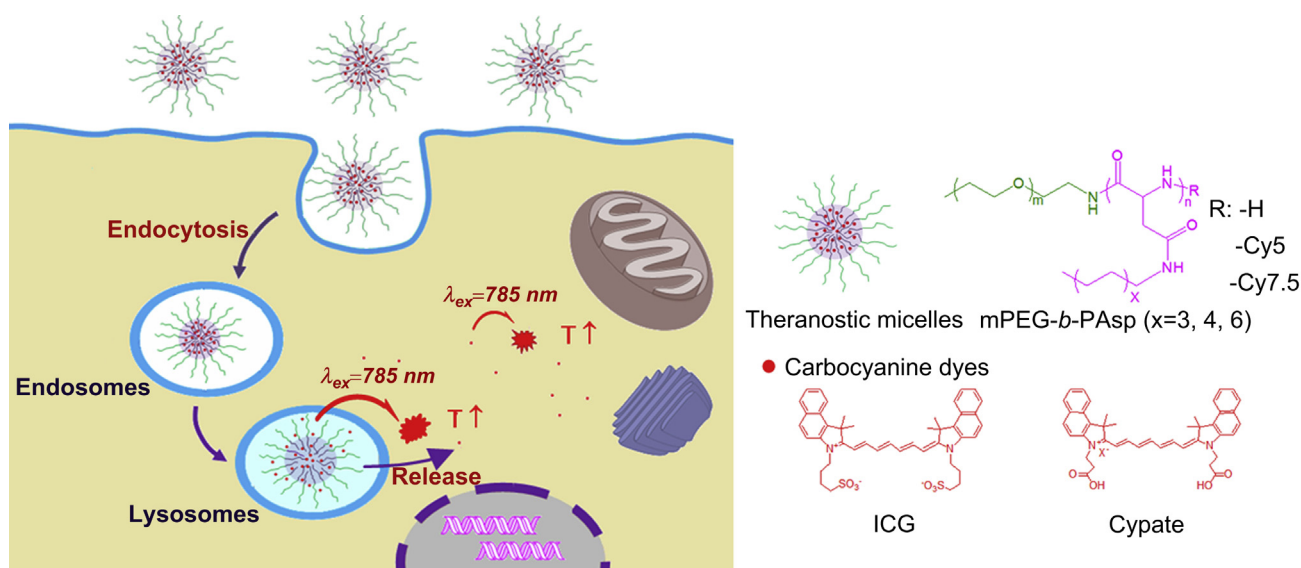
The drug release behavior of ICG from ICG-OA-M, ICG-DA-M and ICG-TA-M containing 0.3 mg ICG was evaluated using dialysis method and free ICG (0.3 mg in DMSO) was used as the control. The drug release was performed in air Constant Temperature Oscillator shaker at 37 °C. 100 mL PBS (0.2 M, pH 7.4) was used as the release medium, respectively. The samples (1.0 mL) were taken after 1, 2, 4, 8, and 16 h with the replacement of an equal volume of fresh medium. The samples were analyzed using a UV–vis spectrometer.

### 2.5. Photothermal effect

The micelle solutions (each 0.5 mL) encapsulating various concentrations of Cypate in vials were irradiated at the excitation wavelength of 785 nm (1.5 W/cm<sup>2</sup>, FS-Optics, China). Simultaneously, the temperature of the solution was monitored during 300 s.

### 2.6. Cellular uptake

A549 cells were seeded on six-well culture plates (1 × 10<sup>5</sup> cells/well) and incubated overnight in DMEM containing 10% FBS. Free ICG and ICG-DA-M (10 µg/mL ICG) were applied to the wells, respectively. After 6 and 24 h incubation, the medium was removed and the cells were washed 3 times using PBS. The cells were incubated with 0.5 mL of trypsin (Sigma–Aldrich, USA) for 3 min at 37 °C, and then counted after centrifuge collection. The counted cells were lysed under ultrasonication and then ICG was further extracted using methanol from the cells. Finally, the concentrations of ICG were measured using a UV–vis spectrometer. The results are presented as a mean and standard deviation obtained from 6 samples. The cellular uptakes of free Cypate and Cy-DA-M were evaluated according to the same procedure.



**Scheme 1.** Schematic illustration of theranostic micelles for prolonged cancer imaging and photothermal therapy of carbocyanine dyes.

### 2.7. Intracellular distribution

Intracellular localization of Cy5-labeled ICG-DA-M in A549 cells was observed using CLSM (Leica). A549 cells ( $1 \times 10^4$  cells/well) were seeded on glass slides in 35-mm dishes using 1.0 mL DMEM. Subsequently, Cy5-labeled ICG-DA-M was added into the medium for 4 h incubation. Then, Hoechst 33342 (10  $\mu$ L) and LysoTracker Green DND-26 (20  $\mu$ L) were used to stain nucleus and endosomes/lysosomes for 3 min, respectively. After the medium was washed, the cells were observed using CLSM.

### 2.8. MTT assay

A549 cells were incubated with the copolymer at different concentrations for 6 h and 24 h, and then the cells were washed with PBS and further incubated for 24 h before subjected to MTT assay. For photothermal cytotoxicity of Cy-DA-M, the cells were incubated with Cy-DA-M at various concentrations for 6 h, and then suffered from 5 min photoirradiation (1.0 W/cm<sup>2</sup>). Subsequently, the cell viability was measured using MTT assay.

### 2.9. Trypan blue staining

To validate cell injury, A549 cells were seeded overnight in 24-well plates and then treated with PBS and Cy-DA-M at the concentration of 20.0  $\mu$ g/mL for 24 h, respectively. Then, the cells were incubated with fresh medium and then exposed to a 785 nm laser for 5 min at 1.0 W/cm<sup>2</sup>. After 1 h, the cells were washed 3 times using PBS, followed by the addition of 0.2 mL trypan blue solution (0.1 wt %). Then, A549 cells were observed using an optical microscope after wash. Trypan blue dye molecules can easily penetrate plasma membranes of dead cells to stain the nuclei, but viable cells cannot be stained.

### 2.10. AO staining

To monitor the disruption of lysosomal membranes, AO was utilized as an intracellular indicator of acidic organelle integrity in A549 cells. AO is a meta-chromatic fluorophore that becomes charged and is retained by proton trapping within acidic compartments. When normal cells were excited with blue light, AO in lysosomes emits an intense red fluorescence, while AO in nuclei and cytosol displays green fluorescence. Upon acidic compartments such as lysosomes is disrupted, the red fluorescence from AO disappears and only green fluorescence can be observed. In this study, A549 cells were seeded overnight on glass slides in 35-mm dishes, and treated with PBS and Cy-DA-M at the concentrations of 0.5, 1.0 and 2.0  $\mu$ g/mL Cypate for 6 h, respectively. Then, the cells were incubated in fresh medium, followed by 5 min photoirradiation at 1.0 W/cm<sup>2</sup>. After 1 h, the cells were washed using PBS and fixed for 10 min using 1.0 mL mixture of methanol/glacial acetic acid (3:1). Then, A549 cells were washed using PBS and further incubated with 6  $\mu$ M AO (1.0 mL) for 15 min. The cells were washed 3 times with PBS before subjected to fluorescence microscopy observation with the excitation wavelength of 488 nm, and emission wavelengths from 515 to 545 nm (green) and from 610 to 640 nm (red).

### 2.11. Biodistribution

A549 cells ( $5 \times 10^6$  cells/each mouse) were subcutaneously injected into the flanks of female BALB/c nude mice (16–18 g) for constructing the tumor-bearing mice. Then, the mice were injected intravenously with free ICG and ICG-DA-M at the dose of 10 mg/kg ICG, respectively. Then, various tissues including heart, liver, spleen, lung, kidney and tumor were extracted from the mice at 24 and 96 h post-injection, respectively. Finally, the tissues were imaged using IVIS Lumina II with the excitation wavelength of 745 nm and the emission wavelength of 820 nm. The NIRF signals from the tissues were calculated to describe the *ex vivo* biodistribution at different time.

### 2.12. In vivo imaging

A549 cells ( $5 \times 10^6$  cells/each mouse) and BxPC-3 cells ( $1 \times 10^7$  cells/each mouse) were subcutaneously injected into the flanks of female BALB/c nude mice (16–18 g) for constructing the mice bearing hypervascular and hypovascular tumors, respectively. ICG-DA-M, free ICG and Cy-DA-M were intravenously into the above mice at the dose of 10 mg/kg ICG or Cypate, respectively. Then, the mice were imaged using IVIS Lumina II with the excitation wavelength of 745 nm and the emission wavelength of 820 nm at 0.16, 1, 2, 4, 6, and 8 day post-injection. For the imaging of Cy7.5-DA-M, the mice were imaged at 24 h and 96 h post-injection using the similar procedure. The average NIRF intensity at tumor was calculated to describe the photon signals of the probes at tumor.

### 2.13. In vivo efficacy

Female BALB/c nude mice (16–18 g) were used for the *in vivo* efficacy evaluation. Briefly, A549 cells ( $5 \times 10^6$  cells/each mouse) were subcutaneously transplanted into the flanks of female mice ( $n = 3$ ). When the tumors reached a size of 50–70 mm<sup>3</sup> (about 10 days after transplantation), Cy-DA-M were injected intravenously into the

mice at a dose of 10 mg/kg Cypate on day 0, 2, and 4, respectively. Subsequently, the tumors were then exposed to photoirradiation for 5 min at the wavelength of 785 nm at 24 h post-injection (1.0 W/cm<sup>2</sup>). The tumor volumes were measured to evaluate the antitumor activity of various groups. The tumor volume (*V*) was calculated as follows:  $V = L \times W^2/2$ , where *W* and *L* are the tumor measurements at the widest and longest points, respectively. The mice were sacrificed by cervical dislocation under anesthetic status after the experiments. The statistic difference was analyzed using *t*-test where *P* values of <0.05 is considered significant. For constructing hepatic murine H22 tumor, H22 cells were harvested from ascites of the mice and then were transplanted into the female BALB/c nude mice ( $1 \times 10^6$  cells/each mouse). When the tumors were allowed to grow for 3–5 days (approximately 70–90 mm<sup>3</sup>), the mice were treated as the above procedures ( $n = 4$ ).

## 3. Results and discussion

### 3.1. Synthesis, preparation and characterization

Polymeric micelles are clinically promising nanocarrier for cancer-targeted delivery [21,25–27], owing to their multiple advantages such as sustained release, prolonged circulation, enhanced permeability and retention (EPR) effect [28,29]. In particular, the micelles possess a core-shell structure, which allows us to screen optimal hydrophobic segments of copolymers for encapsulating anticancer drugs or imaging probes [28–31]. We chose biodegradable polyaspartamide as the copolymer backbone in the consideration of biocompatibility requirements and versatile modification of hydrophobic segments [32]. Monomethoxy poly(ethylene glycol)-*b*-poly(L-aspartic acid) (mPEG-*b*-PAsp) was synthesized by ring-opening polymerization of  $\beta$ -benzyl L-aspartate *N*-carboxy-anhydride (BLA-NCA) with mPEG-NH<sub>2</sub> (12 kDa) (Scheme S1). NMR confirmed the chemical structure of the copolymer (Fig. S1) and gel permeation chromatography measurement also evidenced this synthesis ( $M_w/M_n = 1.08$ ,  $M_w = 30,531$ ). In order to achieve good encapsulation and sustained release of carbocyanine dye, we screened alkylamines with different chain lengths including octylamine (OA), decylamine (DA), and tetradecylamine (TA), which were respectively grafted into the backbones of copolymers via aminolysis for the synthesis of mPEG-*b*-PAsp(OA), mPEG-*b*-PAsp(DA), and mPEG-*b*-PAsp(TA) (Figs. S2–S4). These polymers exhibited the critical micelle concentration (CMC) values of 1.2, 2.3, and 4.6  $\mu$ g/mL, respectively (Fig. S5), and were subsequently used to assemble with ICG into ICG-loaded mPEG-*b*-PAsp(OA) micelles (ICG-OA-M), mPEG-*b*-PAsp(DA) micelles (ICG-DA-M), and mPEG-*b*-PAsp(TA) micelles (ICG-TA-M), respectively. ICG-OA-M had much higher diameter compared to the others (Fig. 1A). ICG-DA-M had the smallest diameter of 41.4 nm with the polydispersity index of 0.09 possibly owing to the formation of the most compact micellar cores consisting of PAsp(DA), and also displayed a spherical morphology (Fig. 1B). We further examined the entrapment efficiency of ICG-DA-M using the centrifuge tubes with 100 kDa membrane filters.  $94.0\% \pm 0.7\%$  ICG was found to be entrapped within the micelles, indicating that the majority of ICG was entrapped within the micelles at the drug loading of 20%, which are superior to those of existing nanoparticles [15,16,20]. Possibly, the grafted medium alkyl chains in the segment of poly(L-aspartic acid) has good affinity with carbocyanine structure, which may allow a large amount of ICG molecules to locate at the micellar cores. The stability of ICG-DA-M in aqueous solution was also evaluated at 4 °C and 25 °C. The micelles had good fluorescent stability during 48 h compared to free ICG (Fig. 1C), which may ascribe to the perfect encapsulation of ICG within the micelles, leading to low interaction of ICG with solvent radicals and ions in aqueous environment [16,33,34].

Drug release often plays a prerequisite factor for achieving their biological application. We evaluated the release profiles of ICG from ICG-OA-M, ICG-DA-M and ICG-TA-M in PBS (pH 7.4) at 37 °C. All the micelles only resulted in the release of about 10% ICG in 4 h

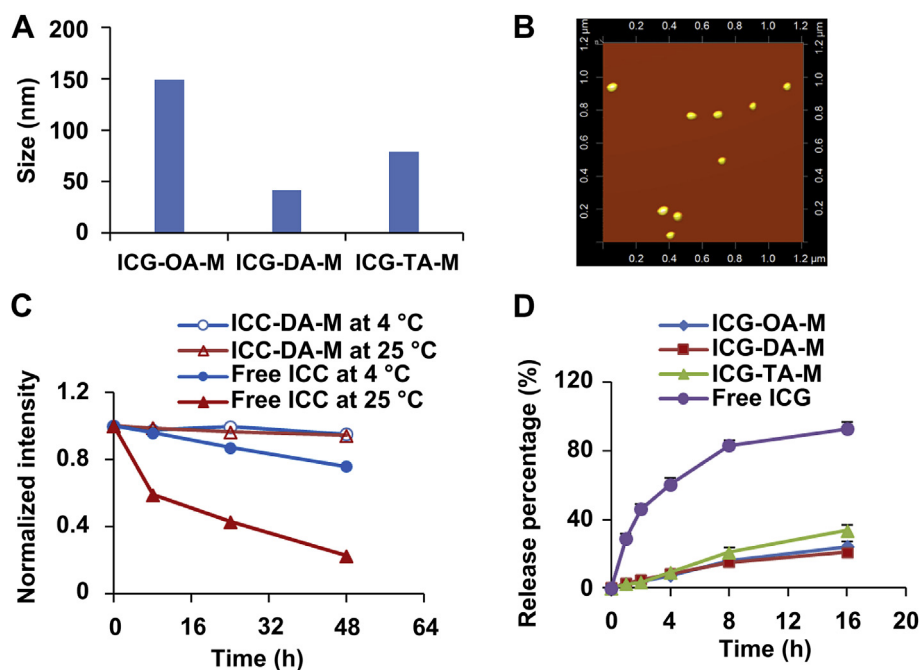


**Fig. 1.** Characterization of theranostic micelles including (A) Particle size of ICG-OA-M, ICG-DA-M and ICG-TA-M, (B) AFM image of ICG-DA-M, (C) Normalized NIRF intensity of ICG-DA-M and free ICG solution at 5  $\mu\text{g}/\text{mL}$  in aqueous solution at the excitation wavelength of 785 nm at 4 °C and 25 °C, respectively, and (D) Accumulative release profiles of ICG from various micelles and free ICG at pH 7.4.

(Fig. 1D), while free ICG as the control had the quick release of 64% ICG in 4 h. The micelles exhibited a significant sustained release capability compared to free ICG. Especially, ICG-DA-M exhibited the slowest release rate during 16 h, indicating that the micelles consisting of mPEG-*b*-PAsp(DA) are preferable to reduce undesirable drug release in blood circulation.

### 3.2. Cytotoxicity, cellular uptake and intracellular distribution

We further evaluated the cytotoxicity of mPEG-*b*-PAsp(DA) using MTT assay. The copolymer in the range of 5–160  $\mu\text{g}/\text{mL}$  had no significant change in cell viability against A549 cells after 6 h and 24 h incubation, indicating that the copolymer has no obvious cytotoxicity (Fig. 2A). To date, several formulations consisting of poly(amino acid)-based copolymers are under clinical trials [25], implying that this type of copolymer is promising as clinically acceptable material.

We demonstrated the cellular uptake capability of ICG-DA-M by cancer cells. ICG-DA-M caused 3-fold and 5-fold increase of the

cellular uptake of ICG after 6 h and 24 h incubation respectively compared to free ICG (Fig. 2B), indicating that the micelles can easily be internalized by cancer cells. We further employed confocal laser scanning microscopy (CLSM) to observe the intracellular distribution of Cy5-labeled ICG-DA-M in A549 cells stained by LysoTracker Green DND-26. The micelles themselves were mainly distributed into endosomes/lysosomes, and exhibited a colocalization percentage of about 75% (Fig. 3), indicating that the enhanced cellular uptake might allow more micelles to be internalized into endosomes/lysosomes and potentially accumulate at tumor [35].

### 3.3. In vivo distribution

To demonstrate the *in vivo* tumor selectivity of the micelles, we prepared empty mPEG-*b*-PAsp(DA)-Cy7.5 micelles (Cy7.5-DA-M) without the encapsulation of ICG, and subsequently injected Cy7.5-DA-M into A549 tumor-bearing nude mice. Fig. 4A shows that the micelles were effectively distributed into tumor at 24 h post-

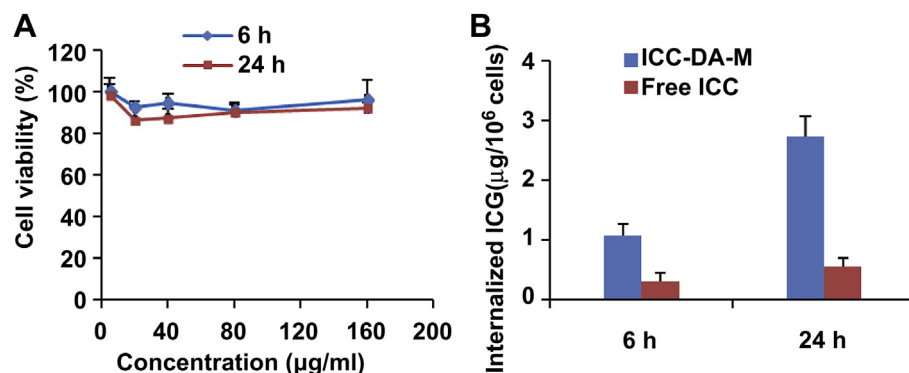


**Fig. 2.** (A) Cell viability of mPEG-*b*-PAsp(DA) after 6 h and 24 h incubation with A549 cells in the range of 5–160  $\mu\text{g}/\text{mL}$ . (B) Amounts of internalized ICG by A549 cells after 6 h and 24 h incubation.



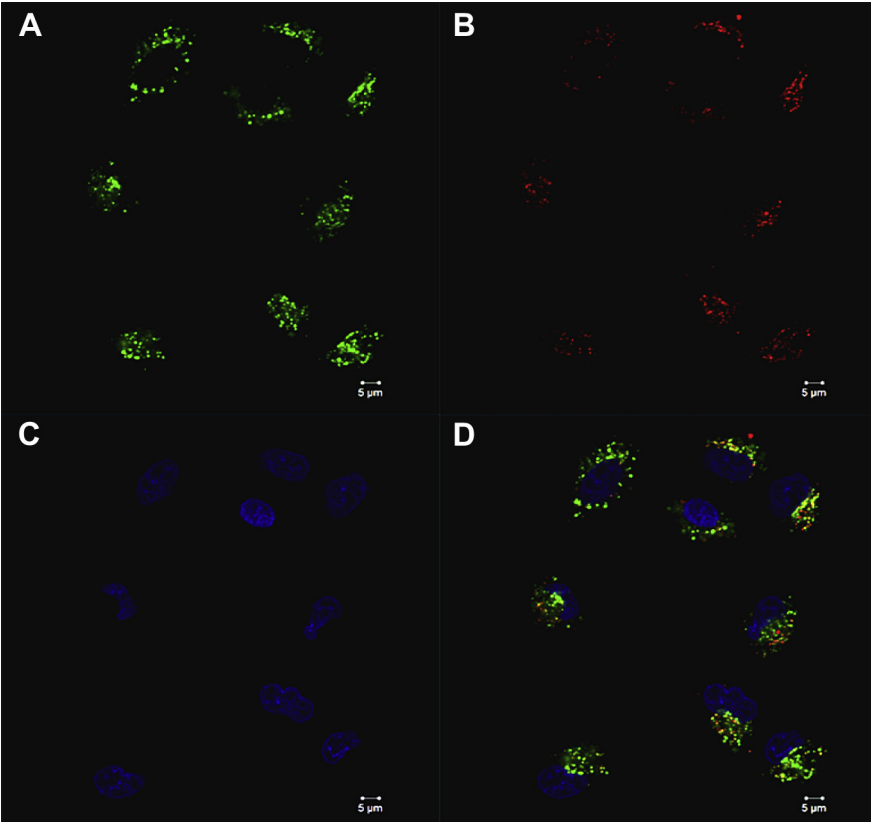


**Fig. 3.** Intracellular distribution of Cy5-labeled ICG-DA-M in A549 cells after 4 h incubation using CLSM. (A) Green fluorescence of endosomes/lysosomes stained by lysoTracker Green DND26, (B) Red fluorescence of Cy5 in Cy5-labeled ICG-DA-M, (C) Blue fluorescence of nucleus stained by Hoechst 33342, and (D) Co-localization of Cy5-labeled ICG-DA-M in endosomes/lysosomes (yellow fluorescence). (For interpretation of the references to color in this figure legend, the reader is referred to the web version of this article.)

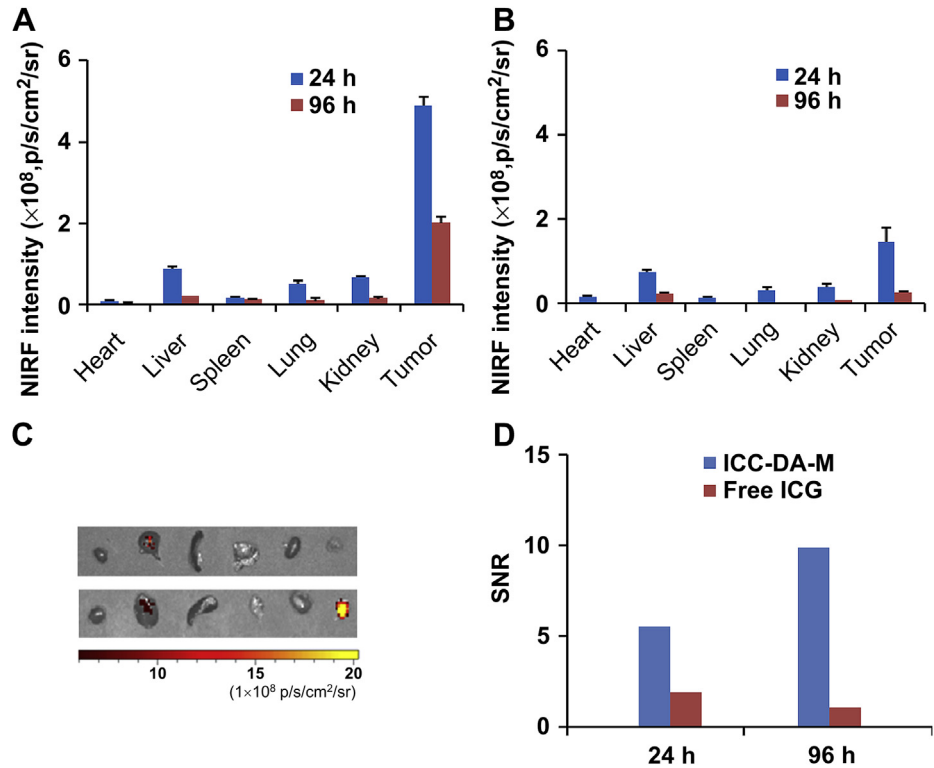


**Fig. 4.** (A) NIRF intensities of ICG-DA-M at heart, liver, spleen, lung, kidney, and tumor of the mice at 24 h and 96 h post-injection at the dose of 10 mg/kg ICG. (B) NIRF intensities of free ICG in heart, liver, spleen, lung, kidney, and tumor of the mice at 24 h and 96 h post-injection at the dose of 10 mg/kg ICG. (C) Ex vivo imaging of heart, liver, spleen, lung, kidney and tumor from the mice bearing tumor treated with free ICG (upper) and ICG-DA-M (bottom) at the dose of 10 mg/kg ICG at 96 h post-injection, respectively. (D) SNR of ICG-DA-M and free ICG at 24 and 96 h post-injection.

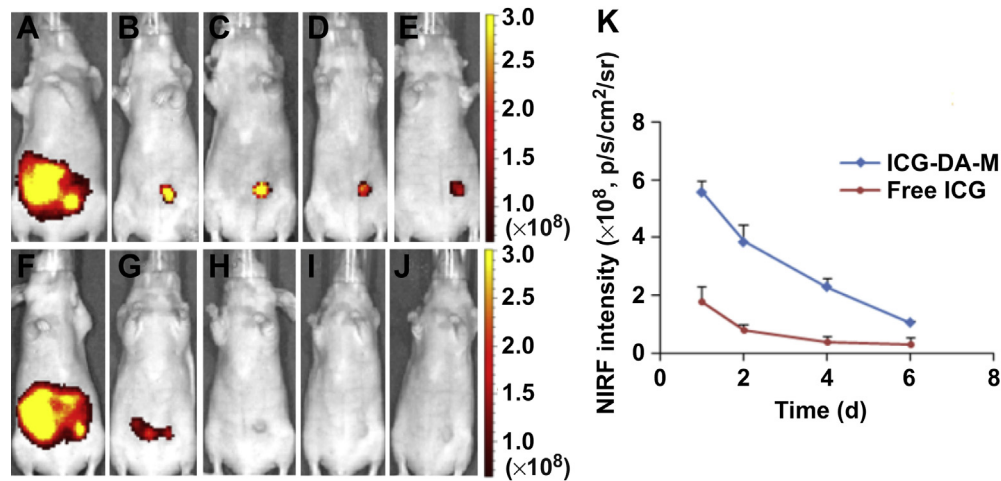


**Fig. 5.** *In vivo* NIRF imaging of the mice bearing A549 tumor injected with ICG-DA-M (A–E) and free ICG (F–J) at the dose of 10 mg/kg ICG on 0.17, 1, 2, 4 and 6 day post-injection respectively, and their NIRF intensity profiles at tumors (K).

injection and also maintained a good retention of NIRF signals at tumor at 96 h post-injection (Fig. S6A). The micelles exhibit preferable distribution and slow elimination at tumor, which might attribute to EPR effect and thereof targeting capacity [15,21]. It indicates that the empty micelles possess good passive targeting capacity, which might potentially improve the accumulation of encapsulated agent (e.g. ICG) at tumor site.

To examine the biodistribution behavior of ICG-DA-M, we intravenously injected ICG-DA-M and free ICG into the mice bearing A549 tumor and monitored their *ex vivo* NIRF at various tissues at 24 h and 96 h post-injection using *in vivo* NIRF imaging. ICG-DA-M and free ICG were mainly distributed into tumor, liver, lung and kidney at 24 h post-injection (Fig. 4B and C). ICG-DA-M resulted in 2.7-fold increase of the accumulation of ICG at tumor compared to free ICG, resulting from EPR effect of the micelles [20,21]. Interestingly, ICG-DA-M still exhibited a detectable NIRF signals at tumor at 4 d post-injection (Fig. 4B and C), but free ICG had obvious elimination and thereof weak NIRF signals at tumor (Fig. S6B). Additionally, most NIRF signals from both ICG-DA-M and free ICG were quickly attenuated at normal tissues after 24 h, and were mostly eliminated at 96 h post-injection. The elimination of ICG at normal tissues is generally considered to be primarily

performed by hepatobiliary system within several hours and finally excreted into the bile. We further defined the ratio of the NIRF signals at tumor to the noise at liver as SNR according to Fig. 4B and C [15,20]. ICG-DA-M display significant SNR increase of ICG from 2.9 to 9.7 during the imaging period of 4 d owing to the quick elimination of ICG in liver (Fig. 4D) [15]. It indicates that the micelles are much more capable to improve SNR than free ICG during a long-term imaging period [15]. Generally, the existing NIRF probes are only observed during a short imaging period of less than 48 h. The prolonged retention of ICG-DA-M at tumor and their quick elimination at normal tissues offer an alternative strategy to improve imaging SNR during a prolonged imaging window.

#### 3.4. *In vivo* NIRF imaging of ICG-DA-M on hypervascular and hypovascular tumors

To demonstrate the imaging capacity of ICG-DA-M, we evaluated *in vivo* NIRF imaging of ICG-DA-M on the mice bearing hypervascular A549 tumors. ICG-DA-M were mainly distributed into tumor, liver and gastrointestinal tracts at 4 h post-injection, and then exhibited a significant accumulation of NIRF signals at tumor at 24 h post-injection, which was 3.1 times higher than that

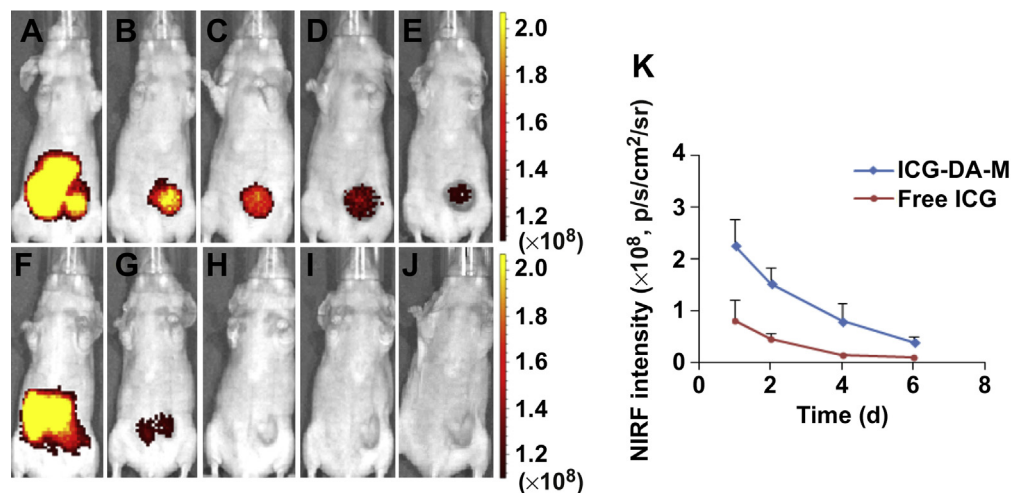


**Fig. 6.** *In vivo* NIRF imaging of the mice bearing BxPC-3 tumor injected with ICG-DA-M (A–E) and free ICG (F–J) at the dose of 10 mg/kg ICG on 0.17, 1, 2, 4 and 6 day post-injection respectively, and their NIRF intensity profiles at tumor (K).

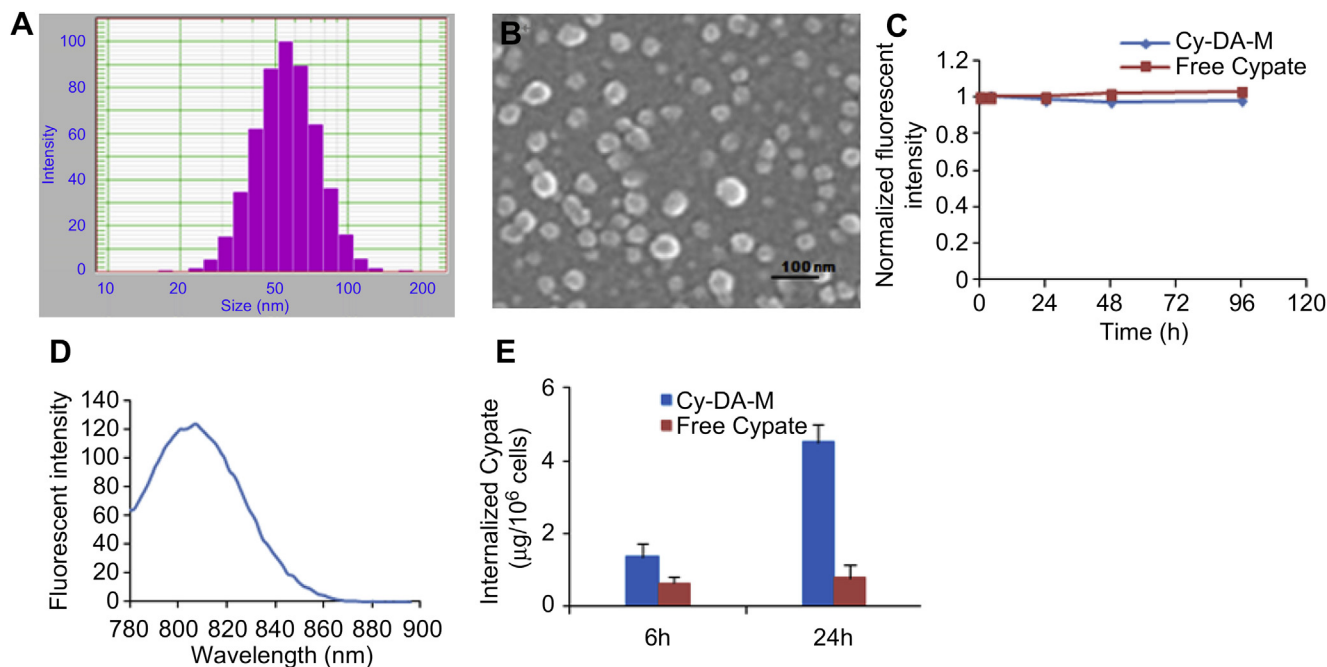


**Fig. 7.** (A) Size distribution of Cy-DA-M. (B) Scanning electron microscopy image of Cy-DA-M (Average SEM size: 42.0 nm). (C) Normalized NIRF intensity of Cypate in the solution of 60% DMSO and Cy-DA-M containing 1.4 μg/mL Cypate at 25 °C, respectively. (D) Emission spectrum of Cy-DA-M at the excitation wavelength of 785 nm. (E) Amounts of internalized Cypate from free Cypate and Cy-DA-M by A549 cells after 6 h and 24 h incubation at the dose of 20 μg/mL Cypate.

from free ICG (Fig. 5A–E and K). In particular, ICG-DA-M still had detectable NIRF signals at tumor during subsequent imaging period of 5 d, accompanying with negligible noise from normal tissues after 24 h post-injection. However, free ICG had a much lower retention of NIRF signals at tumor, leading to its poor ability to probe the tumor (Fig. 5F–J).

Moreover, we also evaluated the *in vivo* imaging of ICG-DA-M on hypovascular BxPC-3 tumor, which is generally considered as a poorly permeable tumor model [21]. ICG-DA-M also exhibited a 2.8-fold increase of accumulation of ICG at tumor compared to free ICG at 24 h, and subsequent long-term retention of detectable NIRF signals at tumor (Fig. 6). Obviously, the micelles can effectively result in the significant targeting of ICG to both hypervascular and hypovascular tumors and subsequent prolonged retention at tumors, which might allow us to detect tumor at a high SNR level.

### 3.5. *In vivo* NIRF imaging of the micelles encapsulating photostable cypate (Cy-DA-M)

However, ICG-DA-M also exhibited gradual attenuation of NIRF signals at both tumors during the imaging period of 6 days (Figs. 5 and 6). We hypothesize that it might attribute to two possibilities including photo-instability or degradation of ICG released from micelles at tumor and the leakage of ICG from tumor. To validate whether the photostability of carbocyanine dye plays a key role in the NIRF attenuation of ICG-DA-M, we further assembled another carbocyanine dye, photostable Cypate into Cypate-loaded mPEG-*b*-PAsp(DA) micelles (Cy-DA-M), which exhibited the drug loading of 50%, average diameter of 57.9 nm, spherical morphology, good aqueous photostability, and enhanced cellular uptake (Fig. 7). Here, photostable Cypate was used to replace photo-instable ICG in the micelles for validating the hypothesis.

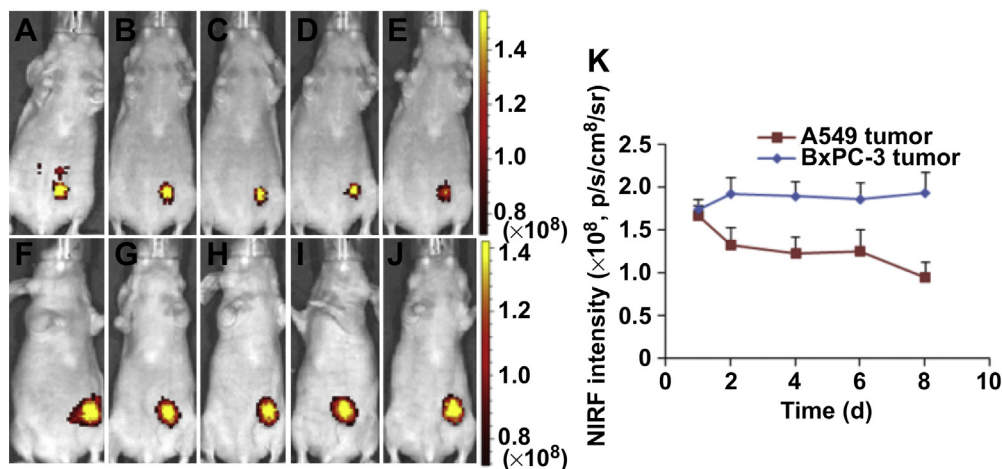


**Fig. 8.** *In vivo* NIRF imaging of the mice bearing A549 tumor (A–E) and BxPC-3 tumor (F–J) injected with Cy-DA-M at the dose of 10 mg/kg Cypate at 1, 2, 4, 6 and 8 day post-injection, respectively, and their NIRF intensity profiles at tumor (K).

Subsequently, we further evaluated the *in vivo* imaging of Cy-DA-M on the mice bearing A549 and BxPC-3 tumors. Cy-DA-M displayed a slight decrease of NIRF signals at A549 tumor during the imaging period of 8 days (Fig. 8A–E), while Cy-DA-M exhibited a more stable retention of NIRF signals at BxPC-3 tumor (Fig. 8F–J). Obviously, Cy-DA-M can generate more stable NIRF signals at both tumors than ICG-DA-M, accompanying with negligible noise. The enhanced stability of signals at tumors possibly ascribed to good photostability of Cypate, whereas the slight decrease at A549 tumor might result from the leakage of Cy-DA-M from permeable A549 tumor. It indicates that Cy-DA-M are highly potential to detect tumor (especially hypovascular tumor) in some major tissues such as liver for cancer imaging. Subsequently, we further evaluated the capacity of Cy-DA-M to achieve photothermal therapy owing to their superior NIRF imaging capacity.

### 3.6. *In vitro* photothermal effect

The preferable accumulation and retention of dyes at tumor play a key prerequisite for subsequent photothermal therapy. To demonstrate photothermal effect of the theranostic micelles as bifunctional agent, we firstly evaluated the photothermal capacity of Cy-DA-M in aqueous solution. The temperature of micelle solution (0.5 mL) was quickly increased from 23 °C to 42 °C in 5 min at the concentration of 2.0 µg/mL Cypate upon photoirradiation and its higher concentrations resulted in more significant increase of temperature (Fig. 9A), while water as the control showed no response to photoirradiation. It indicates that Cy-DA-M may effectively generate hyperthermia, which can potentially trigger cell death when temperature is above 42 °C [5,36].

To examine the photothermal injury of Cy-DA-M on cancer cells, we incubated A549 cells with Cy-DA-M for 24 h, followed by 5 min photoirradiation (1.0 W/cm<sup>2</sup>). Both Cy-DA-M and free Cypate did not induce cell death without photoirradiation (Fig. 9B and C), and the laser irradiation also had no damage on the cells. However, Cy-DA-M effectively caused cell death upon photoirradiation and its IC<sub>50</sub> value was about 12.0 µg/mL (Fig. 9C), which was much lower than that of free Cypate (Fig. 9B). The enhanced cellular uptake and subsequent high enrichment of Cypate within cells might account for the enhanced photothermal cytotoxicity. The cell death was further validated by trypan blue staining the nuclei of dead cells (Fig. 9D), indicating that the cells suffered from severe photothermal injury from Cy-DA-M [11,37].

Generally, photothermal damage on cancer cells results from the destabilization of subcellular organelles such as lysosomes and mitochondria. To demonstrate the destabilization, we further monitored the integrity of lysosomes upon photoirradiation using acridine orange (AO) as an intracellular indicator, which can emit red fluorescence in the intact acidic lysosomes, and display green fluorescence in neutralized cytosol and nuclei. The confocal laser scanning microscopy imaging shows that the acidic lysosomes in A549 cells treated with PBS displayed red fluorescence in the absence of photoirradiation, which was similar to those suffered from photoirradiation (Fig. 10A and E). It indicates that the lysosomal compartments were still stable in the absence of Cypate regardless of photoirradiation. However, the red fluorescence from AO began to be decreased in the presence of Cy-DA-M containing 0.5 µg/mL Cypate upon photoirradiation (Fig. 10B and F), remarkably reduced when the dose of Cypate reached 1.0 µg/mL (Fig. 10C and G), and mostly disappeared at the dose of 2.0 µg/mL (Fig. 10D

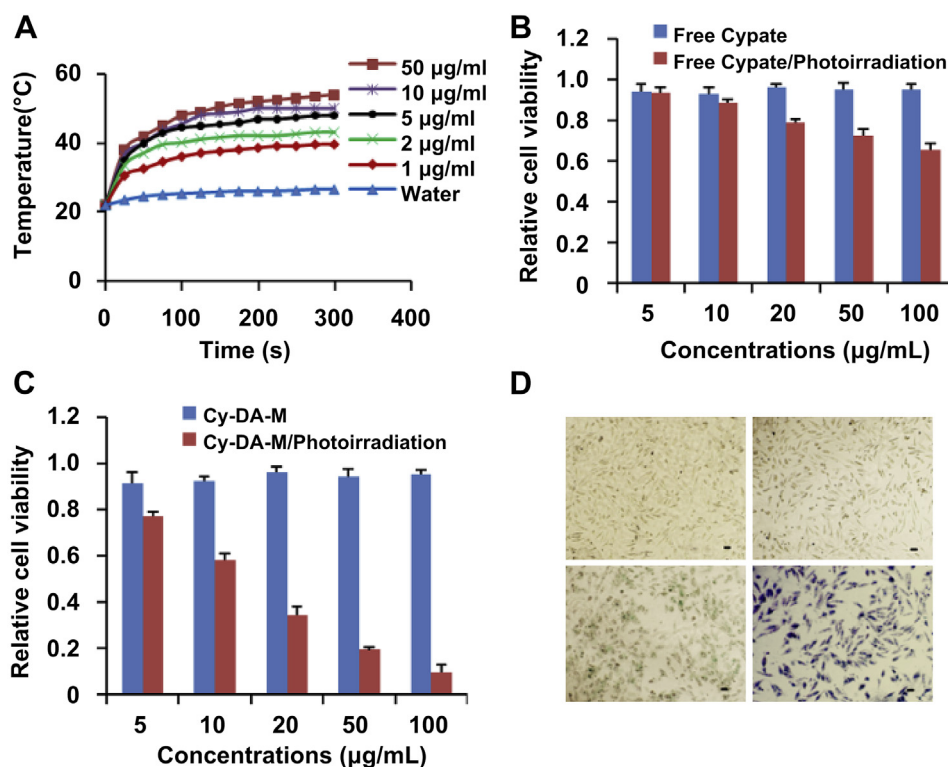


**Fig. 9.** (A) Photothermal effect of Cy-DA-M containing various concentrations of Cypate in aqueous solution (0.5 mL) with 5 min photoirradiation. (B) Relative cell viability of A549 cells after 6 h incubation with free Cypate at different concentrations with or without photoirradiation (5 min, 1.0 W/cm<sup>2</sup>). (C) Relative cell viability of A549 cells after 6 h incubation with Cy-DA-M containing various concentrations of Cypate with and without photoirradiation (5 min, 1.0 W/cm<sup>2</sup>). (D) Trypan blue staining images of A549 cells incubated with PBS without photoirradiation (top left), PBS with 5 min photoirradiation (1.0 W/cm<sup>2</sup>, top right), Cy-DA-M without photoirradiation (bottom left), and Cy-DA-M with 5 min photoirradiation (1.0 W/cm<sup>2</sup>, bottom right) (bar means 10 µm).



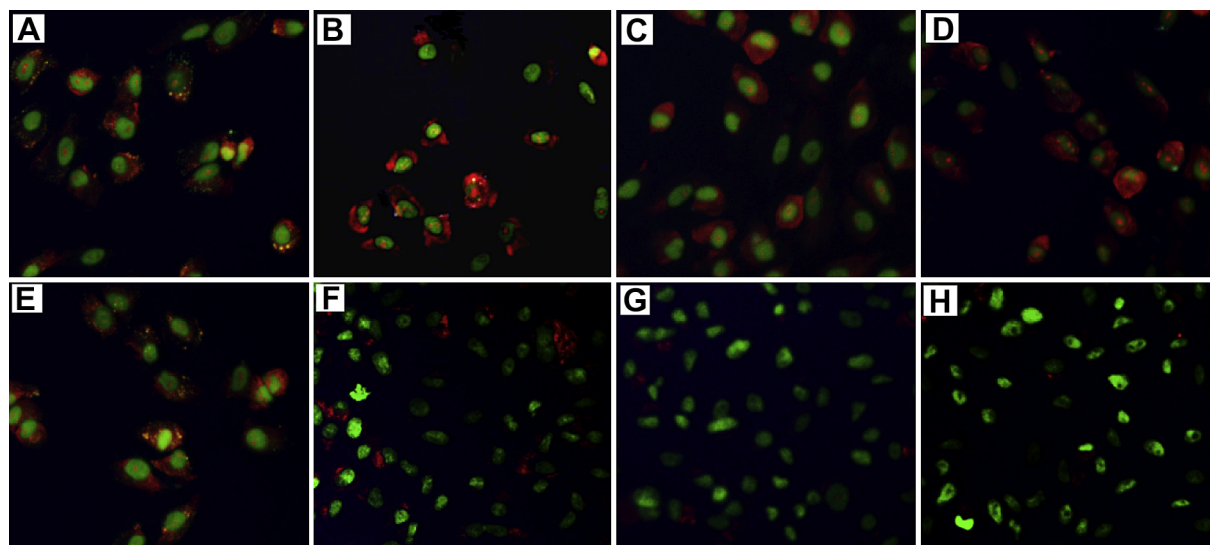


**Fig. 10.** Observation of the lysosomal integrity of A549 cells under 3 min photoirradiation ( $1.0 \text{ W/cm}^2$ ) using AO staining. The cells were respectively treated with PBS (A), Cy-DA-M at the concentrations of  $0.5 \text{ µg/mL}$  Cypate (B),  $1.0 \text{ µg/mL}$  Cypate (C), and  $2.0 \text{ µg/mL}$  Cypate (D) in the absence of photoirradiation. Simultaneously, the cells were also treated with PBS (E), Cy-DA-M at the concentrations of  $0.5 \text{ µg/mL}$  Cypate (F),  $1.0 \text{ µg/mL}$  Cypate (G), and  $2.0 \text{ µg/mL}$  Cypate (H) with 5 min photoirradiation, respectively. AO as an intracellular indicator emits red fluorescence in acidic lysosomes ( $610\text{--}640 \text{ nm}$ , red), and displays green fluorescence in neutralized cytosol and nuclei ( $515\text{--}545 \text{ nm}$ , green). (For interpretation of the references to color in this figure legend, the reader is referred to the web version of this article.)

and H). It indicates that Cy-DA-M at a low dose of Cypate can effectively disrupt lysosomal membranes upon photoirradiation. A few studies have reported that gold nanorods-mediated hyperthermia at a high dose could trigger disruption of lysosomal membranes under very strong irradiation [38]. Cy-DA-M at the dose of as low as  $0.5 \text{ µg/mL}$  Cypate can effectively trigger the destabilization of subcellular organelles, which can account for the photothermal cytotoxicity of Cy-DA-M.

### 3.7. In vivo photothermal efficacy

To elucidate photothermal efficacy of theranostic micelles, Cy-DA-M were injected into the mice bearing A549 tumor at the dose of  $10 \text{ mg/kg}$  Cypate and then the tumors were irradiated at  $1.0 \text{ W/cm}^2$  for 5 min at 24 h post-injection. Subsequently, tumor growth was monitored within 20 days (Fig. 11A). At day 20, the control group without photoirradiation reached an average volume of  $524.4 \pm 88.7 \text{ mm}^3$ , which exhibited 8-fold increase compared to their original volumes. Photoirradiation itself had no significant influence on tumor growth and did not trigger skin damage as well (Fig. S7). Cy-DA-M without photoirradiation had a similar tumor

growth behavior to that of control group, indicating that Cy-DA-M exhibit no therapeutic effect as a nontoxic agent without photoirradiation. However, Cy-DA-M triggered strong tumor necrosis and regression upon photoirradiation, and finally resulted in the ablation of major tumors ( $P < 0.01$ , Fig. 11A and Fig. S7). The necrosis quickly resulted in the generation of scars and subsequently disappeared during the regress. It indicates that Cy-DA-M deliver sufficient Cypate into tumor for achieving hyperthermia and subsequent photothermal effect. Simultaneously, NIR irradiation at the wavelength of  $785 \text{ nm}$  can effectively penetrate into inaccessible tumors for subsequently triggering severe photothermal injury of Cy-DA-M on cancer cells [4]. Moreover, we did not observe any damage of the skins triggered by  $785 \text{ nm}$  photoirradiation.

Furthermore, we further explored the possibility to photothermal therapy of the micelles on aggressive tumor. We evaluated the photothermal effect of Cy-DA-M on the mice bearing aggressive murine hepatic H22 tumor, indicating that Cy-DA-M could also exhibit strong inhibition effect on the growth of aggressive tumor (Fig. 11B,  $P < 0.01$ ). The enhanced cellular uptake and subsequent photothermal damage on cancer cells account for the obvious antitumor efficacy of Cy-DA-M. It indicates that the theranostic

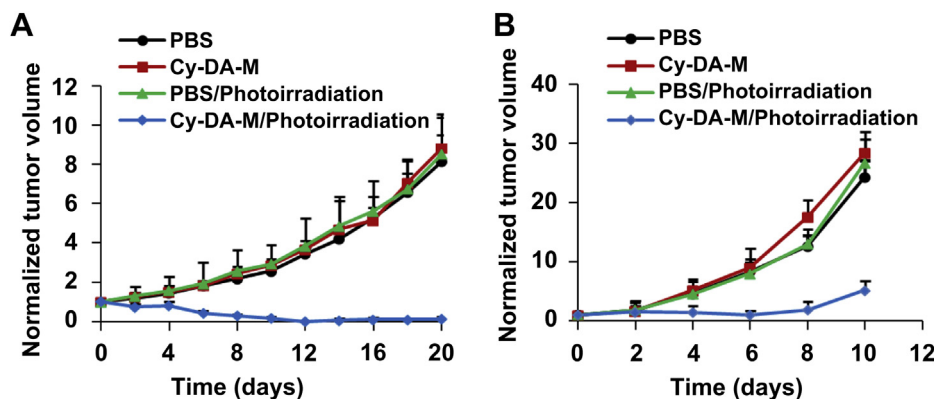


**Fig. 11.** Tumor growth inhibition profiles of Cy-DA-M on the mice bearing A549 tumor (A) and hepatic murine H22 tumor (B) after administration of  $10 \text{ mg/kg}$  Cypate on day 0, 2, and 4, followed by 5 min photoirradiation ( $1.0 \text{ W/cm}^2$ ) at 24 h post-injection.

micelles exhibit superior photothermal therapy on aggressive tumor. In particular, theranostic micelles can provide the ultrasensitive detection of tumor during a prolonged imaging period, which allow us to precisely treat tumor with minimized adverse side effect at normal tissues after imaging [5]. Moreover, photothermal therapy does not require the distribution of carbocyanine dyes into subcellular organelles such as nucleus and mitochondria. Then, the internalized molecules by cancer cells can directly trigger severe photothermal damage via destabilization of subcellular organelles upon photoirradiation. Therefore, the theranostic micelles exhibit multiple advantages for cancer therapy.

#### 4. Conclusions

In this study, we demonstrate a theranostic polyaspartamide micelle system encapsulating bifunctional carbocyanine dyes for long-term cancer NIRF imaging and superior photothermal therapy. The micelles can facilitate cellular uptake, preferable accumulation and long-term retention of carbocyanine dyes at tumors, and simultaneously keep rapid elimination at normal tissues, which cause high imaging SNR at both hypervascular and hypovascular tumors during a prolonged imaging period. In particular, the micelles assembling photostable Cypate can generate superior NIRF imaging contrast during a long-term imaging window compared to those assembling photo-instable ICG. Moreover, the micelles can trigger significant photothermal damage on cancer cells via the destabilization of organelles, leading to successful tumor necrosis and regress upon photoirradiation. We believe that the theranostic micelles are a promising vehicle for efficient cancer imaging and therapy.

#### Acknowledgments

This work was supported by National Basic Research Program (2012CB932500, 2014CB931903), National Natural Science Foundation of China (81202472, 51225305, 81273462), and the priority academic program development of Jiangsu higher education institutions (PAPD).

#### Appendix A. Supplementary data

Supplementary data related to this article can be found at <http://dx.doi.org/10.1016/j.biomaterials.2013.08.022>.

#### References

- [1] Gindy ME, Prud'homme RK. Multifunctional nanoparticles for imaging, delivery and targeting in cancer therapy. *Expert Opin Drug Deliv* 2009;6:865–78.
- [2] Yu MK, Park J, Jon S. Targeting strategies for multifunctional nanoparticles in cancer imaging and therapy. *Theranostics* 2012;2:3–44.
- [3] Cabral H, Nishiyama N, Kataoka K. Supramolecular nanodevices: from design validation to theranostic nanomedicine. *Acc Chem Res* 2011;44:999–1008.
- [4] Mitsunaga M, Ogawa M, Kosaka N, Rosenblum LT, Choyke PL, Kobayashi H. Cancer cell-selective in vivo near infrared photoimmunotherapy targeting specific membrane molecules. *Nat Med* 2011;17:1685–91.
- [5] Jang B, Park JY, Tung CH, Kim IH, Choi Y. Gold nanorod-photosensitizer complex for near-infrared fluorescence imaging and photodynamic/photothermal therapy in vivo. *ACS Nano* 2011;5:1086–94.
- [6] Kosuge H, Sherlock SP, Kitagawa T, Dash R, Robinson JT, Dai H, et al. Near infrared imaging and photothermal ablation of vascular inflammation using single-walled carbon nanotubes. *J Am Heart Assoc* 2012;1:e002568.
- [7] Lovell JF, Jin CS, Huynh E, Jin H, Kim C, Rubinstein JL, et al. Porphyrin nanovesicles generated by porphyrin bilayers for use as multimodal biophotonic contrast agents. *Nat Mater* 2011;10:324–32.
- [8] Melancon MP, Zhou M, Li C. Cancer theranostics with near-infrared light-activatable multimodal nanoparticles. *Acc Chem Res* 2011;44:947–56.
- [9] Zheng X, Xing D, Zhou F, Wu B, Chen WR. Indocyanine green-containing nanostructure as near infrared dual-functional targeting probes for optical imaging and photothermal therapy. *Mol Pharmacol* 2011;8:447–56.
- [10] Almutairi A, Guillaudeu SJ, Berezin MY, Achilefu S, Frechet JM. Biodegradable pH-sensing dendritic nanoprobe for near-infrared fluorescence lifetime and intensity imaging. *J Am Chem Soc* 2008;130:444–5.
- [11] Yu J, Javier D, Yaseen MA, Nitin N, Richards-Kortum R, Anvari B, et al. Self-assembly synthesis, tumor cell targeting, and photothermal capabilities of antibody-coated indocyanine green nanocapsules. *J Am Chem Soc* 2010;132:1929–38.
- [12] Zhang Z, Achilefu S. Design, synthesis and evaluation of near-infrared fluorescent pH indicators in a physiologically relevant range. *Chem Commun* 2005:5887–9.
- [13] Liu TW, Chen J, Burgess L, Cao W, Shi J, Wilson BC, et al. Multimodal bacteriochlorophyll theranostic agent. *Theranostics* 2011;1:354–62.
- [14] Lovell JF, Liu TW, Chen J, Zheng G. Activatable photosensitizers for imaging and therapy. *Chem Rev* 2010;110:2839–57.
- [15] Miki K, Kimura A, Oride K, Kuramochi Y, Matsuoka H, Harada H, et al. High-contrast fluorescence imaging of tumors in vivo using nanoparticles of amphiphilic brush-like copolymers produced by ROMP. *Angew Chem Int Ed* 2011;50:6567–70.
- [16] Kirchherr AK, Briel A, Mader K. Stabilization of indocyanine green by encapsulation within micellar systems. *Mol Pharmacol* 2009;6:480–91.
- [17] Luo S, Zhang E, Su Y, Cheng T, Shi C. A review of NIR dyes in cancer targeting and imaging. *Biomaterials* 2011;32:7127–38.
- [18] Escobedo JO, Rusin O, Lim S, Strongin RM. NIR dyes for bioimaging applications. *Curr Opin Chem Biol* 2010;14:64–70.
- [19] Wang J, Moore J, Laulhe S, Nantz M, Achilefu S, Kang KA. Fluorophore-gold nanoparticle complex for sensitive optical biosensing and imaging. *Nanotechnology* 2012;23:095501.
- [20] Altinoglu EI, Russin TJ, Kaiser JM, Barth BM, Eklund PC, Kester M, et al. Near-infrared emitting fluorophore-doped calcium phosphate nanoparticles for in vivo imaging of human breast cancer. *ACS Nano* 2008;2:2075–84.
- [21] Cabral H, Matsumoto Y, Mizuno K, Chen Q, Murakami M, Kimura M, et al. Accumulation of sub-100 nm polymeric micelles in poorly permeable tumors depends on size. *Nat Nanotechnol* 2011;6:815–23.
- [22] Anraku Y, Kishimura A, Oba M, Yamasaki Y, Kataoka K. Spontaneous formation of nanosized unilamellar polyion complex vesicles with tunable size and properties. *J Am Chem Soc* 2010;132:1631–6.
- [23] Ye Y, Bloch S, Kao J, Achilefu S. Multivalent carbocyanine molecular probes: synthesis and applications. *Bioconjug Chem* 2004;16:51–61.
- [24] Ye Y, Li WP, Anderson CJ, Kao J, Nikiforovich GV, Achilefu S. Synthesis and characterization of a macrocyclic near-infrared optical scaffold. *J Am Chem Soc* 2003;125:7766–7.
- [25] Murakami M, Cabral H, Matsumoto Y, Wu S, Kano MR, Yamori T, et al. Improving drug potency and efficacy by nanocarrier-mediated subcellular targeting. *Sci Trans Med* 2011;3:64ra2.
- [26] Matsumura Y. Poly (amino acid) micelle nanocarriers in preclinical and clinical studies. *Adv Drug Deliv Rev* 2008;60:899–914.
- [27] Matsumura Y. Preclinical and clinical studies of NK012, an SN-38-incorporating polymeric micelles, which is designed based on EPR effect. *Adv Drug Deliv Rev* 2011;63:184–92.
- [28] Gong J, Chen M, Zheng Y, Wang S, Wang Y. Polymeric micelles drug delivery system in oncology. *J Control Release* 2012;159:312–23.
- [29] Kedar U, Phutane P, Shidhaye S, Kadam V. Advances in polymeric micelles for drug delivery and tumor targeting. *Nanomed-Nanotechnol* 2010;6:714–29.
- [30] Torchilin VP. Micellar nanocarriers: pharmaceutical perspectives. *Pharm Res* 2007;24:1–16.
- [31] Nishiyama N, Kataoka K. Current state, achievements, and future prospects of polymeric micelles as nanocarriers for drug and gene delivery. *Pharmacol Ther* 2006;112:630–48.
- [32] Bae Y, Kataoka K. Intelligent polymeric micelles from functional poly(ethylene glycol)-poly(amino acid) block copolymers. *Adv Drug Deliv Rev* 2009;61:768–84.
- [33] Gao Y, Chen Y, Ji X, He X, Yin Q, Zhang Z, et al. Controlled intracellular release of doxorubicin in multidrug-resistant cancer cells by tuning the shell-pore sizes of mesoporous silica nanoparticles. *ACS Nano* 2011;5:9788–98.
- [34] Babin J, Pelletier M, Lepage M, Allard J-F, Morris D, Zhao Y. A new two-photon-sensitive block copolymer nanocarrier. *Angew Chem Int Ed* 2009;48:3329–32.
- [35] Maxfield FR, McGraw TE. Endocytic recycling. *Nat Rev Mol Cell Biol* 2004;5:121–2.
- [36] You J, Zhang G, Li C. Exceptionally high payload of doxorubicin in hollow gold nanospheres for near-infrared light-triggered drug release. *ACS Nano* 2010;4:1033–41.
- [37] Huang P, Lin J, Wang X, Wang Z, Zhang C, He M, et al. Light-triggered theranostics based on photosensitizer-conjugated carbon dots for simultaneous enhanced-fluorescence imaging and photodynamic therapy. *Adv Mater* 2012;24:5104–10.
- [38] Zhang Z, Wang L, Wang J, Jiang X, Li X, Hu Z, et al. Mesoporous silica-coated gold nanorods as a light-mediated multifunctional theranostic platform for cancer treatment. *Adv Mater* 2012;24:1418–23.